

Competing Ultrafast Energy Relaxation Pathways in Photoexcited Graphene

S.A. Jensen,^{1,2} Z. Mics,¹ I. Ivanov,¹ H.S. Varol,¹ D. Turchinovich,¹
F.H.L. Koppens,^{3,*} M. Bonn,^{1,*} and K.J. Tielrooij^{3,*}

¹Max Planck Institute for Polymer Research, Ackermannweg 10, 55128 Mainz, Germany

²FOM Institute AMOLF, Amsterdam, Science Park 104, 1098 XG Amsterdam, Netherlands

³ICFO - Institut de Ciències Fotòniques, Mediterranean Technology Park, Castelldefels (Barcelona) 08860, Spain

For most optoelectronic applications of graphene a thorough understanding of the processes that govern energy relaxation of photoexcited carriers is essential. The ultrafast energy relaxation in graphene occurs through two competing pathways: carrier-carrier scattering – creating an elevated carrier temperature – and optical phonon emission. At present, it is not clear what determines the dominating relaxation pathway. Here we reach a unifying picture of the ultrafast energy relaxation by investigating the terahertz photoconductivity, while varying the Fermi energy, photon energy, and fluence over a wide range. We find that sufficiently low fluence ($\lesssim 4 \mu\text{J}/\text{cm}^2$) in conjunction with sufficiently high Fermi energy ($\gtrsim 0.1 \text{ eV}$) gives rise to energy relaxation that is dominated by carrier-carrier scattering, which leads to efficient carrier heating. Upon increasing the fluence or decreasing the Fermi energy, the carrier heating efficiency decreases, presumably due to energy relaxation that becomes increasingly dominated by phonon emission. Carrier heating through carrier-carrier scattering accounts for the negative photoconductivity for doped graphene observed at terahertz frequencies. We present a simple model that reproduces the data for a wide range of Fermi levels and excitation energies, and allows us to qualitatively assess how the branching ratio between the two distinct relaxation pathways depends on excitation fluence and Fermi energy.

Graphene is a promising material for, amongst others, photo-sensing and photovoltaic applications [1], owing to its broadband absorption [2, 3], its high carrier mobility [4, 5] and the ability to create a photovoltage from heated electrons or holes [6]. It furthermore uniquely allows for electrical control of the carrier density and polarity [4]. To establish the potential and limitations of graphene-based optoelectronic devices, a thorough understanding of the ultrafast (sub-picosecond) primary energy relaxation dynamics of photoexcited carriers is essential. For undoped graphene (with Fermi energy $E_F \approx 0$), ultrafast energy relaxation through interband carrier-carrier scattering was predicted [7] and observed [8, 9] to lead to multiple electron-hole pair excitation. For doped graphene (with Fermi energy $|E_F| > 0$), ultrafast energy relaxation through carrier-carrier interaction also plays an important role, with intraband scattering leading to carrier heating [10–13]. In addition, the ultrafast energy relaxation was ascribed to optical phonon emission [14, 15], which reduces the carrier heating efficiency. Closely related, for undoped graphene the sign of the terahertz (THz) photoconductivity is positive (see e.g. [16–19]), whereas for intrinsically doped graphene the sign is negative, meaning that photoexcitation gives rise to an apparent decrease of conductivity [11, 16, 17, 20–22]. This negative photoconductivity was attributed to stimulated THz emission [20], and to a reduction of the intrinsic conductivity by enhanced scattering with optical phonons [21, 22] or by carrier heating [11, 16, 17]. Since the experimental

parameters of all these studies differ strongly, different conclusions were drawn regarding the dominating energy relaxation pathway and the origin of the sign of the THz photoconductivity.

Here, we reach a unifying picture of the energy relaxation of photoexcited carriers in graphene by experimentally studying the ultrafast energy relaxation of photoexcited carriers for a large parameter space, where we vary the Fermi energy and the fluence. We compare the data with a simple model of carrier heating, which quantitatively reproduces the frequency-dependent THz photoconductivity for a large range of Fermi energies and fluences with a single free fit parameter. This fit parameter is the carrier heating efficiency, i.e. the fraction of absorbed energy from incident light that is transferred to the electron system. Although the THz photoconductivity is not a direct probe of the carrier temperature, and the model parameters carry some uncertainty, this approach allows us to identify qualitatively how the ultrafast energy relaxation processes depend on excitation fluence and Fermi energy.

We study the ultrafast carrier-energy relaxation using time-resolved THz spectroscopy experiments, where an excitation pulse with a wavelength of 400, 800 or 1500 nm (corresponding to a photon energy of $E_0 = 3.10$, 1.55 or 0.83 eV, respectively) excites electron-hole pairs, and a low-energy terahertz (THz, $f = 0.3 - 2 \text{ THz}$) probe pulse interrogates the sample, where it interacts with mobile carriers. An optical delay line controls the relative time delay between excitation and probe pulses,

*Electronic address: klaas-jan.tielrooij@icfo.es, bonn@mpip-mainz.mpg.de, frank.koppens@icfo.es

making it possible to determine the photo-induced change in conductivity (the photoconductivity $\Delta\sigma$) as a function of time with a time resolution of ~ 150 fs [23]. We use two different samples: The first sample, where the graphene has a controllable Fermi energy, contains Chemical Vapor Deposition (CVD) grown graphene with an area of 1 cm^2 transferred onto a substrate that consists of doped silicon, covered by a 300 nm thick layer of SiO_2 . The silicon serves as the backgate for electrical control of the Fermi energy (carrier doping) of the graphene sheet from $E_F = 0.3$ eV down to ~ 0.06 eV (the width of the neutrality region is ~ 0.06 eV, see Supp. Info). We use weakly doped silicon (resistivity of 10-20 Ωcm) and sufficiently low pump energy (0.83 eV) to ensure that the photo-induced signal from the silicon in the substrate (without graphene) is minimized (See Supp. Info). Two silver-pasted electrical contacts to the graphene sheet enable resistance measurements to retrieve the Fermi energy through the capacitive coupling of the backgate (See Supp. Info). The second sample contains CVD grown graphene with an area of a square inch transferred onto SiO_2 with a fixed Fermi level of < 0.15 eV (see Supp. Info). We carefully measure the fluence F as described in Ref. [24] and use the experimentally determined optical absorption of graphene on SiO_2 using standard UV-Vis spectrometry to obtain the absorbed fluence F_{abs} , and from this the number of absorbed photons $N_{\text{exc}} = F_{\text{abs}}/E_0$, which is equal to the number of primary excited carriers.

To investigate the ultrafast (sub-picosecond) energy relaxation dynamics of photoexcited carriers, we first examine the temporal evolution of the photoconductivity. In Fig. 1a we show the dynamics for a range of Fermi energies using the sample with controllable Fermi energy, and in Fig. 1b for a range of fluences using the sample with fixed Fermi energy. We find that all traces, except the one with Fermi energy within the neutrality region width ($E_F < 0.06$ eV), show negative photoconductivity with a sub-picosecond rise, followed by a picosecond decay. Similar pump-probe dynamics have been observed before [11, 16–22] and can be understood as follows: During the rise of the signal three main processes take place: (i) the creation of initial electron-hole pairs; and subsequent ultrafast energy relaxation through two competing relaxation channels, namely (ii) carrier-carrier scattering and (iii) optical phonon emission. Thus, the peak signal corresponds to a 'hot state' with an elevated carrier temperature T_{el} and/or more energy in optical phonons [8, 10–15]. During the subsequent picosecond decay, the 'hot state' cools down to the same state as before photoexcitation. The fraction of absorbed energy that – after the initial ultrafast energy relaxation – ends up in the electron system or in the phonon system depends on the timescales associated with carrier heating and phonon emission, respectively.

The ultrafast energy relaxation takes place during the first few hundred femtoseconds after photoexcitation, i.e. during the rise of the conductivity change. Figs. 1c and 1d show the normalized photoconductivity signals for this time window. We will discuss the evolution of the signal amplitude as a function of Fermi energy and fluence later. First we note that the rise dynamics exhibit an intriguing effect: upon decreasing the Fermi energy (i.e. the density of intrinsic carriers N_{int}) or increasing the fluence (i.e. the density of primary excited carriers N_{exc}) the signal peak is reached at increasingly later times. To quantify these results, we describe the dynamics using two rise times and an exponential decay time. The two rise times allow for part of the conductivity change to occur with the (fixed) experimental time resolution and part with a (free) slower time scale. We then examine the effective rise time τ_{rise} , which is the amplitude-weighted average of the two (see Methods). The insets of Fig. 1c and Fig. 1d show τ_{rise} as a function of N_{int} and N_{exc} , respectively. Indeed, for decreasing N_{int} and increasing N_{exc} the effective rise time increases from below 200 fs (limited by the experimental time resolution) up to 400 fs (for $E_F < 0.1$ eV).

The slowing down of the ultrafast energy relaxation of photoexcited carriers with decreasing Fermi energy is consistent with energy relaxation through intraband carrier-carrier scattering (see bottom right inset in Fig. 1c). The microscopic picture of this scattering process is shown for two different Fermi energies in the top left inset of Fig. 1c. Photoexcited carriers relax by exchanging energy with intrinsic conduction band carriers that thus heat up. The amount of energy that is exchanged between photoexcited carriers and intrinsic conduction band carriers in each intraband carrier-carrier scattering event is $\sim E_F$ [10]. Therefore, if E_F decreases, more energy-exchange events are required for the photoexcited carriers to complete their energy relaxation cascade and therefore the relaxation time will increase (see bottom right inset of Fig. 1c). If the energy relaxation through carrier-carrier scattering would slow down in such a way that the relaxation rate becomes comparable to the rate of other relaxation channels (e.g. optical phonon emission), we expect these channels to start contributing to the overall energy relaxation. This would lead to a decrease in the fraction of energy that is transferred to the electron system, i.e. a reduced carrier heating efficiency.

We quantify the fraction of absorbed energy that leads to carrier heating by comparing our THz photoconductivity data with the results of a simple thermodynamic model. In short, carrier heating leads to a broader carrier distribution (higher T_{el}), which – in combination with an energy-dependent scattering time [25, 26] – leads to the photo-induced change in THz conductivity (see Methods). The carrier heating is governed by the amount of absorbed energy F_{abs} and the electronic heat

capacity of graphene, which for a degenerate electron gas is given by $C_{\text{el}} = \alpha T_{\text{el}}$ [27]. Here $\alpha = \frac{2\pi E_F k_B^2}{3\hbar^2 v_F}$, with \hbar , v_F and k_B the reduced Planck constant, the Fermi velocity and Boltzmann's constant, respectively. The possibility of controlling the Fermi energy of graphene thus allows for tunability of the heat capacity (see Fig. 2a), which in turn determines the 'hot' carrier temperature T'_{el} that the system reaches. Figure 2b shows that T'_{el} is equivalently determined by both the fluence and the Fermi energy.

To calculate the 'hot' carrier temperature we use a basic numerical approach, which produces a heat capacity in the degenerate regime that corresponds well with the analytical heat capacity (see Fig. 2a), while remaining valid for non-degenerate electron temperatures ($k_B T_{\text{el}} > E_F$). The numerical approach is based on the concept that before photoexcitation there is a known amount of energy in the electronic system: $\mathcal{E}_1 = \int_0^\infty d\epsilon D(\epsilon) \epsilon F(E_F, T_{\text{el}})$; and a known number of carriers in the conduction band: $N_{\text{int}} = \int_0^\infty d\epsilon D(\epsilon) F(E_F, T_{\text{el}})$, where $D(\epsilon)$ is the energy-dependent density of states and $F(E_F, T_{\text{el}})$ is the Fermi-Dirac distribution that depends on Fermi energy E_F and carrier temperature T_{el} . Due to optical excitation, an amount of energy F_{abs} is absorbed in the graphene and a fraction η of this energy ends up in the electronic system through intraband carrier-carrier scattering. After intraband heating is complete, the system is then described by the following set of equations: $\mathcal{E}_2 = \mathcal{E}_1 + \eta F_{\text{abs}} = \int_0^\infty d\epsilon D(\epsilon) \epsilon F(E'_F, T'_{\text{el}})$, and (conserving the number of conduction band carriers) $N_{\text{int}} = \int_0^\infty d\epsilon D(\epsilon) F(E'_F, T'_{\text{el}})$. Here E'_F and T'_{el} are the chemical potential and the carrier temperature in the 'hot state', respectively. Carrier heating thus alters the carrier distribution, where we find by numerically solving the equations for \mathcal{E}_2 and N_{int} that the carrier temperature increases and the chemical potential decreases by photoexcitation (see inset of Fig. 2c and Methods). The photo-induced increase of carrier temperature, and the associated decrease in chemical potential were experimentally confirmed recently [13].

The hot carrier distribution, with E'_F and T'_{el} calculated using the carrier heating model, directly leads to negative THz photoconductivity (see Methods), which scales linearly with carrier temperature up to ~ 2000 K and then shows some saturation behavior (Fig. 2c). We test the validity of our carrier heating model by comparing its predictions for the frequency-resolved photoconductivity with our experimental results for the sample with fixed Fermi energy. In Fig. 3a we show this comparison for a fluence of $\sim 12 \mu\text{J}/\text{cm}^2$ (pump wavelength 800 nm, $N_{\text{exc}} = 1 \cdot 10^{12}$ absorbed photons/ cm^2). We compare the data (at the time delay that corresponds to the signal peak) with the model result for a ground state Fermi energy of 0.11 eV and a scattering time proportionality constant of

200 fs/eV (extracted from the Raman spectrum, THz conductivity measurements on the same sample without photoexcitation, and the saturation value of the THz photoconductivity at high fluence; see also Supp. Info) and find good agreement with a heating efficiency of $\eta = 0.75$. The small discrepancies between data and model can be ascribed to artifacts that arise from the temporal change of the photoconductivity during the interaction with the THz pulse [28], although we largely avoid these by moving the optical pump delay line simultaneously with the THz probe delay line.

The overall agreement between data and model shows that the observed negative THz photoconductivity of intrinsically doped graphene [11, 16, 17, 20–22] can be fully reproduced by considering intraband carrier heating, which reduces the thermally averaged conductivity of the intrinsic carriers. Despite the simplicity of the model, it can also explain the experimental results in Ref. [21] using their experimental parameters, as well as the results in Ref. [20], by letting the environmental gas change the Fermi energy. These observations lead us to conclude that, despite some uncertainty in the determination of the Fermi energy and the scattering time, the model is suitable for obtaining reliable qualitative indications on how the carrier heating efficiency depends on the Fermi energy and the fluence.

We now examine the 'high fluence' regime using $N_{\text{exc}} = 8 \cdot 10^{12}$ absorbed photons/ cm^2 (a fluence of $\sim 100 \mu\text{J}/\text{cm}^2$) in Fig. 3b. This corresponds to the regime where the energy relaxation is slower than the experimental time resolution (see Fig. 1d). Here we find that we can only describe the data with a significantly reduced carrier heating efficiency of $\eta \approx 0.5$ (keeping the ground state Fermi energy and scattering time proportionality constant the same as in the low fluence regime). Combined, these results show that at sufficiently low fluence, a large fraction of the absorbed energy ends up in the electron system, i.e. the ultrafast energy relaxation occurs through efficient (and fast) carrier-carrier scattering. However, upon increasing the fluence (i.e. the carrier temperature), the relative amount of energy transferred to the electron system decreases, which means that carrier-carrier scattering becomes less efficient (and slower) and other relaxation processes start to contribute.

To determine in more detail how the carrier heating efficiency depends on fluence, we study the peak photoconductivity of the sample with fixed Fermi energy for a large range of excitation powers, for both 800 nm and 400 nm excitation. We show the photoconductivity at the peak (when the ultrafast energy relaxation is complete) in Fig. 4a-b, together with the results of the carrier heating model for the same parameters as in Fig. 3a and a frequency of 0.7 THz. For low fluences (up to $\sim 4 \mu\text{J}/\text{cm}^2$, corresponding to $N_{\text{exc}} \sim 0.3 \cdot 10^{12}$ absorbed

photons/cm², 800 nm excitation, $\sim 2\%$ absorption) the experimental data are in agreement with the heating model with a fixed heating efficiency of $\eta = 1$. We notice that the calculated photoconductivity shows saturation behavior with N_{exc} even for constant η . This is related to the nonlinear dependence of the THz photoconductivity on carrier temperature (Fig. 2c). Interestingly, at fluences above $\sim 4 \mu\text{J}/\text{cm}^2$ the experimental photoconductivity starts saturating and the model is only in agreement for a heating efficiency that gradually decreases to $\sim 50\%$ for the highest fluences applied here (Fig. 4a). These observations suggest that once a certain carrier temperature (~ 4000 K, see inset Fig. 4b) is reached, the heating efficiency decreases. Interestingly, the experimental data for excitation with 400 nm light start deviating from the model (with efficient heating) at $N_{\text{exc}} \sim 0.15 \cdot 10^{12}$ absorbed photons/cm² (Fig. 4b), instead of $\sim 0.3 \cdot 10^{12}$ absorbed photons/cm² in the case of excitation with 800 nm light. This is because each 400 nm photon has twice the energy of a 800 nm photon. Thus, in both cases the carrier heating efficiency starts decreasing around the same carrier temperature.

We now determine how the heating efficiency depends on the Fermi energy by measuring the peak photoconductivity for the sample with controllable Fermi energy as a function of both excitation power and Fermi energy. The combined results (for excitation at 1500 nm) are represented in Fig. 5a, where we show the peak photoconductivity as a function of gate voltage for five different excitation powers. In Fig. 5b we show the peak photoconductivity as a function of N_{exc} for three distinct gate voltages, corresponding to $N_{\text{int}} \approx 1, 2$ and $3 \cdot 10^{12}$ carriers/cm², and compare these to the results of the heating model. We find that for a doping of $N_{\text{int}} = 3 \cdot 10^{12}$ carriers/cm² ($E_F \sim 0.2$ eV) the data is in good agreement with the carrier heating model, using a scattering time proportionality constant of ~ 50 fs/eV and a carrier heating efficiency of $\eta = 1$. However, for the lowest N_{int} , which corresponds to a Fermi energy of ~ 0.1 eV, we find a carrier heating efficiency of $\sim 20\%$, using the same energy-dependent scattering time. These results are in good agreement with the observed slowdown of the rise dynamics with decreasing Fermi energy in Fig. 1b.

Comparing the data and the heating model leads to the following physical picture of the ultrafast energy relaxation in graphene: Until a certain carrier temperature is reached (~ 4000 K), the ultrafast energy relaxation is dominated by carrier-carrier scattering, which leads to efficient and fast (< 150 fs) carrier heating. Once this carrier temperature is reached, the relaxation slows down and the carrier heating efficiency decreases, as ultrafast energy relaxation occurs through additional pathways involving optical phonon emission [14]. The reduction in heating efficiency that follows from the macroscopic heating model can be explained using the microscopic

picture of intraband carrier-carrier scattering, as put forward in Refs. [10, 11]. At increased electron temperatures, the (quasi-equilibrium) Fermi energy decreases (see Methods), which means that the electronic heat capacity decreases. It furthermore implies that the amount of energy that is exchanged in intraband carrier-carrier scattering events ($\sim E_F$) decreases. Therefore, energy relaxation of a photoexcited carrier requires an increasing number of intraband carrier-carrier scattering cascade steps. Thus for an increasing carrier temperature, energy relaxation through intraband carrier heating slows down.

The physical picture of carrier-temperature dependent ultrafast energy relaxation of photoexcited carriers in graphene unites the conclusions of a large fraction of the existing literature on this topic. For example in Ref. [14], with excitation in the 'high fluence' regime ($\sim 10^{14}$ absorbed photons/cm² at 800 nm), it was concluded from the experimentally measured carrier temperature that only part of the absorbed light energy ends up in the electronic system, whereas the rest couples to optical phonons. An ultrafast optical pump-probe study employing a fluence of $200 \mu\text{J}/\text{cm}^2$ [15], also in the 'high fluence' regime, similarly demonstrated optical phonon mediated relaxation, in addition to carrier heating. By measuring in the 'low fluence' regime (a few μJ 's), Ref. [11] concluded that the ultrafast energy relaxation was dominated by carrier heating. Furthermore, two very recent optical pump - THz probe studies [16, 17] both used an excited carrier density of $N_{\text{exc}} \approx 1 \cdot 10^{12}$ absorbed photon/cm² at 800 nm and ascribe their observed negative THz photoconductivity (partially) to carrier heating.

In conclusion, we provide a unifying explanation of the ultrafast energy relaxation of photoexcited carriers in graphene. For sufficiently low excitation power and sufficiently high Fermi energy, the relaxation is dominated by carrier-carrier scattering, which leads to efficient generation of hot carriers. This regime typically persists up to a fluence of $\sim 4 \mu\text{J}/\text{cm}^2$ (or $N_{\text{exc}} = 0.3 \cdot 10^{12}$ absorbed 800 nm photons/cm²) for a Fermi energy of 0.1 eV. For larger Fermi energy, a higher fluence can be used without significant reduction in heating efficiency. In the case of lower Fermi energy and/or a higher fluence, the heating efficiency will decrease due to slower intraband carrier-carrier scattering and additional energy relaxation channels involving optical phonon emission. This opens up the possibility to control the pathway of ultrafast energy relaxation, i.e. the ability to tune the efficiency of energy transfer from the primary excited carriers to electronic heat or to alternative degrees of freedom, such as lattice heat. Such tunability is useful for future applications, for instance in the field of photodetection, where hot carriers are the dominant source of photocurrent generation [6]. Finally, we note that the terrestrial solar radiation (on the order of a pJ/cm² during a 10 ps timescale) corresponds to the 'low fluence' regime with efficient carrier heating, which is therefore the relevant process to con-

sider for photovoltaic applications.

METHODS

Photoconductivity from carrier heating model

We use a numerical model based on carrier heating to calculate the complex photoconductivity of photoexcited graphene. The frequency-dependent conductivity of graphene is generally given by [26]

$$\sigma(\omega) = \frac{e^2 v_F^2}{2} \int_0^\infty d\epsilon D(\epsilon) \frac{\tau_{\text{scatter}}(\epsilon)}{1 - i\omega\tau_{\text{scatter}}(\epsilon)} \frac{dF(E_F, T_{\text{el}})}{d\epsilon}, \quad (1)$$

with e the elementary charge, v_F the Fermi velocity, $D(\epsilon) = \frac{2\epsilon}{\pi\hbar^2 v_F^2}$ the density of states, \hbar the reduced Planck constant, $\tau_{\text{scatter}}(\epsilon)$ the energy-dependent momentum scattering time and $F(E_F, T_{\text{el}})$ the Fermi-Dirac distribution that is determined by the Fermi level and the carrier temperature. For unexcited graphene we use the steady state Fermi level E_F and the ambient temperature T_{el} . We furthermore use a scattering time that is determined by charged impurity scattering and increases linearly with energy ϵ [25, 26]. After electron-hole pair excitation of graphene, photoexcited carriers can interact with the intrinsic carriers, leading to intraband thermalization (see also main text): the carrier temperature increases to T'_{el} and the chemical potential decreases to E'_F . The reason for the decrease of the chemical potential is the linear scaling of the $D(\epsilon)$ with energy: a broader carrier distribution (higher carrier temperature) would lead to an increased number of carriers in the conduction band, if the Fermi energy would be kept constant. Therefore, a higher carrier temperature leads to a lower Fermi energy, as confirmed experimentally in Ref. [13]. The conductivity of photoexcited graphene $\sigma'(\omega)$ then follows from Eq. 1, using the 'hot Fermi level' and 'hot carrier temperature' with the photoconductivity given by $\Delta\sigma(\omega) = \sigma'(\omega) - \sigma(\omega)$.

Our model takes into account the effect of intraband carrier heating on the photoconductivity through the carrier distribution, which is sufficient to explain the observed negative photoconductivity [11, 16, 17, 20–22] and the dependence on excitation power and Fermi energy. The model does not explicitly include the effect of energy relaxation to optical phonons on the photoconductivity, as proposed in Ref. [22]. This is justified, because for the graphene used here (with an impurity-scattering-limited mobility below 2500 cm²/Vs) the effect of phonons on the conductivity is negligibly small at low fluences [11]. We note that for very high fluences ($N_{\text{exc}} > 10^{12}$ absorbed photons/cm²) and for phonon-scattering-limited graphene with mobilities $> 10,000$ cm²/Vs [29], this effect likely plays a role, in addition to carrier heating. Furthermore, a more advanced model could include de-

viations from linear scaling between the scattering time and the carrier energy [30], as well as changes in the Drude weight. The latter effect occurs when the valence and conduction band electrons no longer have separate thermal distributions and likely plays an important role around the Dirac point, where it correctly produces positive photoconductivity [17].

Rise dynamics

We describe the time-resolved photoconductivity with a phenomenological model that includes a rise step and an exponential decay step with time τ_{decay} . In the low excitation power/high Fermi energy regime (highly efficient carrier heating), the rise occurs within our instrument response function. For high excitation power/low Fermi energy the rise contains a very fast component and a slow component (reduced carrier heating efficiency). Therefore we model the rise dynamics with a 'fast' rise component that is fixed at a value equal to the pulse duration of $\tau_{\text{pulse}} = 120\text{--}150$ fs (depending on the excitation wavelength) and a variable 'slow' rise component τ_{slow} with a longer pulse duration, and describe the time-resolved photoconductivity by

$$-\Delta\sigma(t) = A \cdot \text{Conv}(e^{-t/\tau_{\text{decay}}}, \tau_{\text{pulse}}) + B \cdot \text{Conv}(e^{-t/\tau_{\text{decay}}}, \tau_{\text{slow}}), \quad (2)$$

where A and B are the amplitudes corresponding to the 'fast' and the 'slow' rise components and $\text{Conv}(y(t), \tau)$ means taking the convolution of $y(t)$ with a Gaussian pulse of width τ . The effective rise time is then given by

$$\tau_{\text{rise}} = \frac{A + B}{A/\tau_{\text{pulse}} + B/\tau_{\text{slow}}}. \quad (3)$$

In the fit, the free parameters are A , B , τ_{slow} and τ_{decay} . The resulting effective rise time gives an indication of how fast the initial energy relaxation of photoexcited carriers takes place.

ACKNOWLEDGEMENTS

We would like to thank Justin Song, Leonid Levitov, Sebastien Nanot and Enrique Cánovas for useful discussions. KJT thanks NWO for a Rubicon fellowship. FK acknowledges support by the Fundacio Cellex Barcelona, the ERC Career integration grant 294056 (GRANOP), the ERC starting grant 307806 (CarbonLight) and support by the E. C. under Graphene Flagship (contract no. CNECT-ICT-604391).

-
- [1] Bonaccorso et al., Graphene Photonics and Optoelectronics. *Nature Phot.* **4**, 611 (2010)
- [2] J.M. Dawlaty et al. Measurement of the optical absorption spectra of epitaxial graphene from terahertz to visible. *Appl. Phys. Lett.* **93**, 131905 (2008)
- [3] L. Ren et al., Terahertz and Infrared Spectroscopy of Gated Large-Area Graphene. *Nano Lett.* **12**, 3711 – 3715 (2012)
- [4] K.S. Novoselov et al., Electric field effect in atomically thin carbon films. *Science* **306** 666 – 669 (2004)
- [5] L. Wang et al., One-Dimensional Electrical Contact to a Two-Dimensional Material. *Science* **342** 614-617 (2013)
- [6] N.M. Gabor et al., Hot Carrier-Assisted Intrinsic Photoresponse in Graphene. *Science* **334**, 648-652 (2011)
- [7] Winzer, T. , Knorr, A. & Malić, E. Carrier Multiplication in Graphene. *Nano Lett.* **10**, 4839–4843 (2010).
- [8] D. Brida et al., Ultrafast collinear scattering and carrier multiplication in graphene. *Nature Comm.* **4**, 1987 (2013)
- [9] T. Plötzing et al. *Nano Lett.* **Article ASAP**, DOI 10.1021/nl502114w (2014)
- [10] J.C.W. Song et al., Photoexcited carrier dynamics and impact-excitation cascade in graphene. *Phys. Rev. B* **87**, 155429 (2013)
- [11] K.J. Tielrooij et al., Photoexcitation cascade and multiple hot-carrier generation in graphene. *Nature Phys.* **9**, 248-252 (2013)
- [12] J.C. Johannsen et al., Direct view on the ultrafast carrier dynamics in graphene. *Phys. Rev. Lett.* **111**, 027403 (2013)
- [13] I. Gierz et al., Snapshots of non-equilibrium Dirac carrier distributions in graphene. *Nature Mat.* **12**, 1119-1124 (2013)
- [14] C.H. Lui et al., Ultrafast photoluminescence from graphene. *Phys. Rev. Lett.* **105**, 127404 (2010)
- [15] M. Breusing et al., Ultrafast nonequilibrium carrier dynamics in a single graphene layer. *Phys. Rev. B* **83**, 153410 (2011)
- [16] S.-F. Shi et al., Controlling Graphene Ultrafast Hot Carrier Response from Metal-like to Semiconductor-like by Electrostatic Gating. *Nano Lett.* **14**, 1578 – 1582 (2014)
- [17] A.J. Frenzel et al., Semiconducting-to-metallic photoconductivity crossover and temperature-dependent Drude weight in graphene. *Phys. Rev. Lett.* **113**, 056602 (2014)
- [18] J.H. Strait et al., Very Slow Cooling Dynamics of Photoexcited Carriers in Graphene Observed by Optical-Pump Terahertz-Probe Spectroscopy. *Nano Lett.* **11**, 4902-4906 (2011)
- [19] P.A. George et al., Ultrafast Optical-Pump Terahertz-Probe Spectroscopy of the Carrier Relaxation and Recombination Dynamics in Epitaxial Graphene. *Nano Lett.* **8** 4248-4251 (2008)
- [20] C.J. Docherty et al., Extreme sensitivity of graphene photoconductivity to environmental gases. *Nature Comm.* **3**, 1228 (2012)
- [21] A.J. Frenzel et al., Observation of suppressed terahertz absorption in photoexcited graphene. *Appl. Phys. Lett.* **102**, 113111 (2013)
- [22] G. Jnawali et al., Observation of a Transient Decrease in Terahertz Conductivity of Single-Layer Graphene Induced by Ultrafast Optical Excitation. *Nano Lett.* **13**, 524–530 (2013)
- [23] R. Ulbricht et al., Carrier dynamics in semiconductors studied with time-resolved terahertz spectroscopy. *Rev. Mod. Phys.* **83**, 543 (2011)
- [24] J.J.H. Pijpers et al., Assessment of carrier-multiplication efficiency in bulk PbSe and PbS. *Nature Phys.* **5**, 811 (2009).
- [25] T. Ando, Screening Effect and Impurity Scattering in Monolayer Graphene. *J. Phys. Soc. Jpn.* **75**, 074716 (2006)
- [26] S. Das Sarma, S. Adam, E. H. Hwang, and E. Rossi, Electronic transport in two-dimensional graphene. *Rev. Mod. Phys.* **83**, 407 (2011)
- [27] C. Kittel, *Introduction to Solid State Physics*, Wiley and Sons (2005)
- [28] E. Hendry et al., Interchain effects in the ultrafast photo-physics of a semiconducting polymer: THz time-domain spectroscopy of thin films and isolated chains in solution. *Phys. Rev. B* **71**, 125201 (2005)
- [29] V. Perebeinos and P. Avouris, Inelastic scattering and current saturation in graphene. *Phys. Rev. B* **81**, 195442 (2010)
- [30] E. H. Hwang, S. Adam, and S. Das Sarma, Carrier Transport in Two-Dimensional Graphene Layers. *Phys. Rev. Lett.* **98**, 186806 (2007)

I. FIGURES

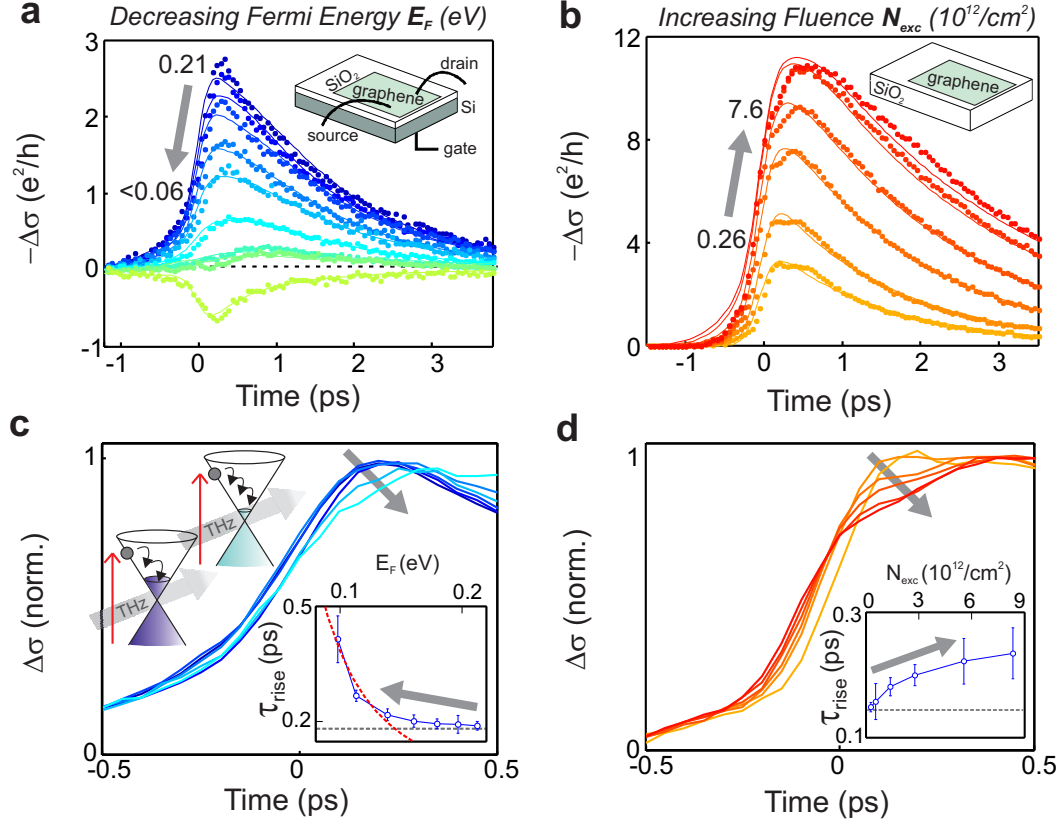


FIG. 1: *Energy relaxation dynamics - dependence on Fermi energy and fluence.* **a)** The time-resolved photoconductivity for nine different gate voltages ($V - V_D = -70, -60, -50, -40, -30, -20, -15, -10$ and 0 V), i.e. for decreasing Fermi energy E_F or intrinsic carrier concentration N_{int} (sample with controllable Fermi energy). The photoconductivity is extracted from the measured change in THz transmission after photoexcitation with 1500 nm light (excitation power corresponds to $N_{exc} = 0.8 \cdot 10^{12}$ absorbed photons/cm²), using the thin film approximation as in Ref. [11]. The inset shows the geometry of the sample, as explained in the text. The photoconductivity is negative for all traces, except for the one closest to the Dirac point, where it is positive. The solid lines are fits with an effective rise time τ_{rise} and an exponential decay time (see Methods). **b)** The time-resolved photoconductivity for excitation with 800 nm light at six different excitation powers, corresponding to absorbed photon densities of $N_{exc} = 0.26, 0.50, 1.2, 2.5, 5.0$ and $7.6 \cdot 10^{12}$ photons/cm² (sample with fixed Fermi energy). The geometry of the sample with a fixed Fermi energy of $E_F \sim 0.1$ eV (see Supp. Info), is shown in the inset and explained in the text. The photoconductivity is negative and increases for increasing excitation power, as the carrier temperature increases. The solid lines are fits with an effective rise time τ_{rise} and an exponential decay time (see Methods). **c)** The photoconductivity normalized to the peak of the signal (sample with controllable Fermi energy), showing that decreasing the Fermi energy leads to slower rise dynamics (i.e. slower energy relaxation). The fitted values for τ_{rise} as a function of N_{int} are shown in the inset, together with the theoretically predicted energy relaxation time based on Ref. [10] (scaled by a factor 1.8) and the experimental time resolution (horizontal dashed line). The schematics in the top left show the ultrafast energy relaxation of a photoexcited carrier for two different Fermi energies, according to the carrier heating process described in Refs. [10, 11]. **d)** The photoconductivity normalized to the peak of the signal (sample with fixed Fermi energy), showing that increasing the excitation power leads to slower rise dynamics. The fitted values for τ_{rise} as a function of N_{exc} are shown in the inset together with the experimental time resolution (horizontal dashed line).

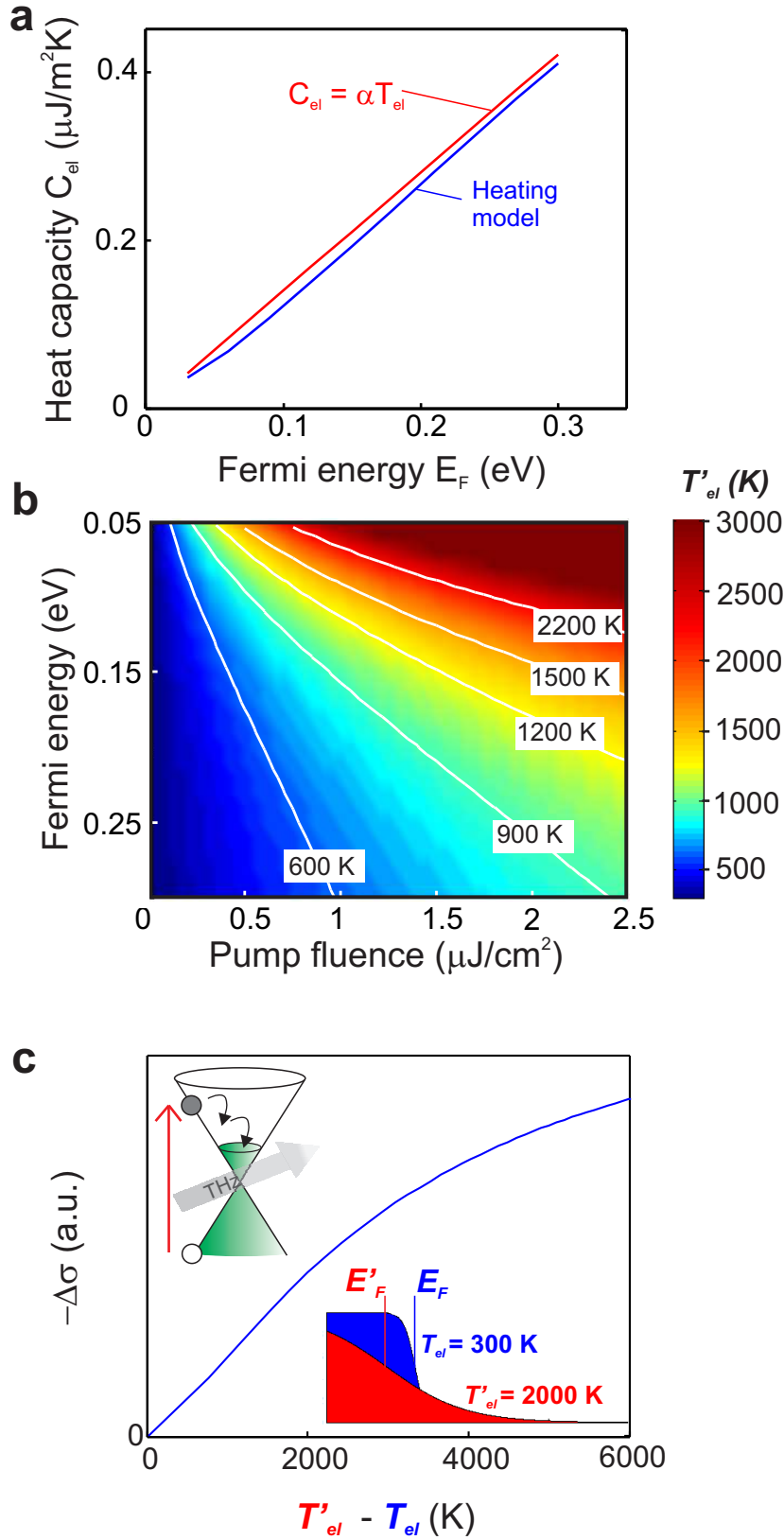


FIG. 2: *Carrier heating model.* **a**) The electronic heat capacity according to the analytical theory (red line) and our numerical model (blue line), showing linear scaling with Fermi energy. **b**) Contour plot of the temperature of the carrier population, showing that decreasing the Fermi energy and increasing the fluence have an equivalent effect on the temperature of the electrons after photoexcitation and intraband thermalization. The carrier temperature is calculated through a simple thermodynamic model (see text). **c**) The calculated negative THz photoconductivity as a function of carrier temperature, showing a linear dependence up to ~ 2000 K. The top left inset shows schematically the process of ultrafast energy relaxation of a photoexcited carrier, which leads to an increase of the carrier temperature from T_{el} to T'_{el} . The inset on the bottom right shows the Fermi-Dirac distribution of the conduction band carriers, where the temperature increase leads to a decrease of the Fermi energy (to keep the total number of conduction band carriers constant).

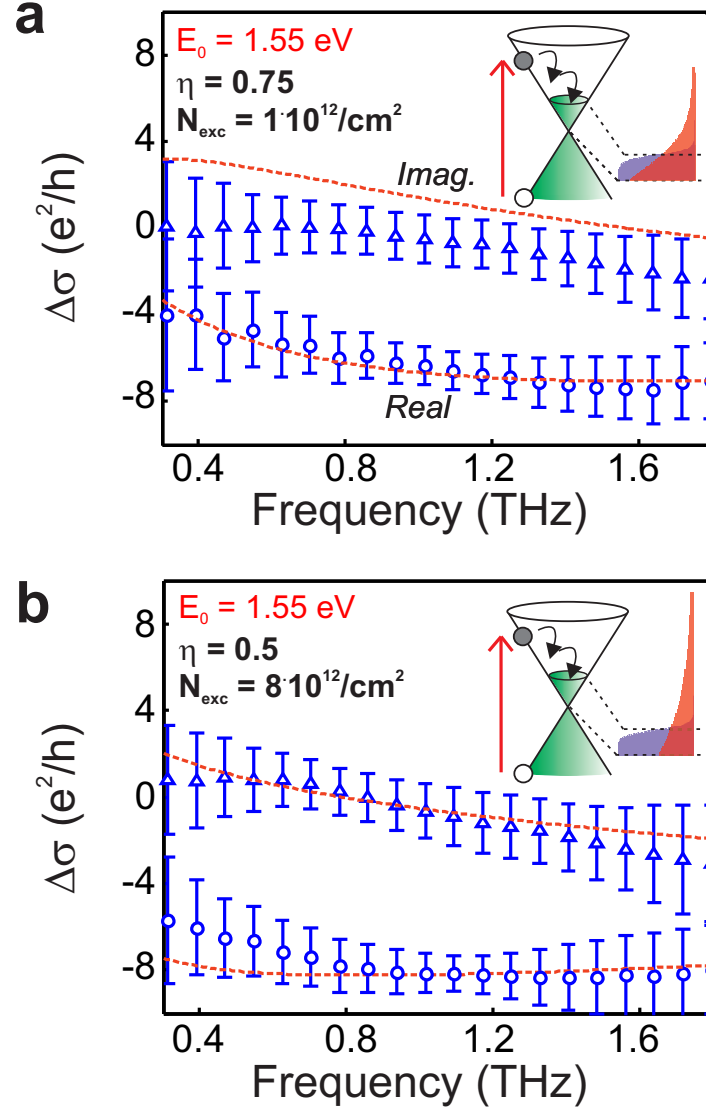


FIG. 3: *Comparison of experimental and theoretical photoconductivity.* **a)** The complex photoconductivity of the sample with fixed Fermi energy as a function of frequency for an excitation fluence corresponding to $N_{\text{exc}} = 1 \cdot 10^{12}$ carriers/cm², together with the model result with a carrier heating efficiency of $\eta = 0.75$. The model (see also main text and Methods) describes the photoconductivity after photoexcited carriers have thermalized through intraband carrier-carrier scattering and directly yields the observed negative photoconductivity. **b)** The complex photoconductivity of the sample with fixed Fermi energy as a function of frequency for an excitation fluence corresponding to $N_{\text{exc}} = 8 \cdot 10^{12}$ carriers/cm², together with the model result with a carrier heating efficiency of $\eta = 0.5$. This shows that in this regime other energy relaxation channels contribute to the ultrafast energy relaxation. The insets in panels **a** and **b** schematically show the process of carrier heating through intraband scattering and the corresponding carrier distributions for the ambient carrier temperature T_{el} (blue) and the elevated carrier temperature T'_{el} after photoexcitation and carrier thermalization (red). The error bars in panels **a** and **b** represent the experimental (non-systematic) error bars (95 % confidence interval).

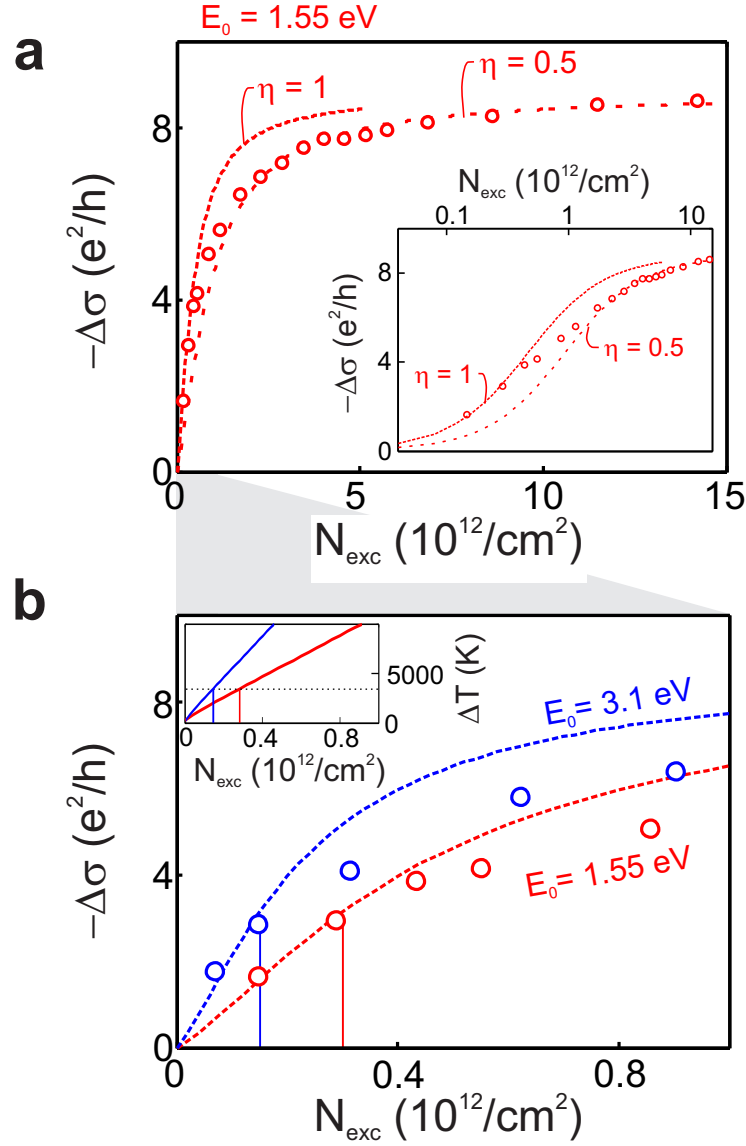


FIG. 4: *Carrier heating efficiency - dependence on fluence.* **a)** The peak photoconductivity of the sample with fixed Fermi energy for a large range of excitation powers and an excitation wavelength of 800 nm together with the model with $\eta = 1$ (short dashed line) and a heating efficiency of $\eta = 0.5$ (long dashed line). The inset shows the same data on a logarithmic horizontal scale. **b)** The peak photoconductivity of the sample with fixed Fermi energy as a function of excitation power (N_{exc}) for excitation with 800 nm light (corresponding to an energy of the primary excited carrier of $E_0/2 = 0.75$ eV) and 400 nm light ($E_0/2 = 1.5$ eV). The dashed lines correspond to the model with the same parameters (Fermi energy and scattering time proportionality constant) as in panel **a**, using $\eta = 1$. The model describes the data well up to $N_{\text{exc}} = 0.3 \cdot 10^{12}$ carriers/ cm^2 for 800 nm excitation and up to $N_{\text{exc}} = 0.15 \cdot 10^{12}$ carriers/ cm^2 for 400 nm excitation. The inset shows the carrier temperature that is reached after excitation and thermalization by carrier-carrier scattering, reaching ~ 4000 K before heating becomes less efficient, for both excitation wavelengths. The symbol size of the data in panels **a** and **b** represents the error.

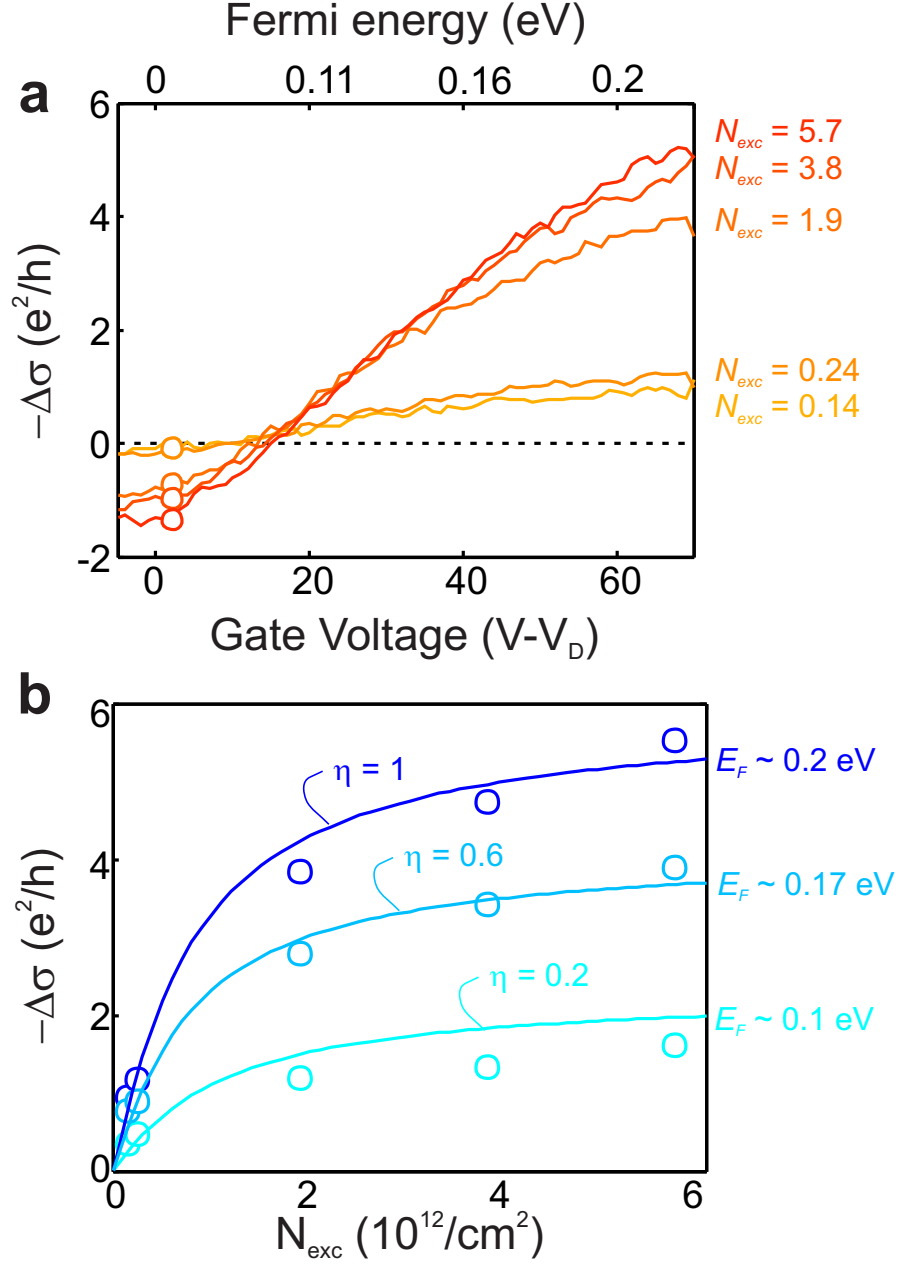


FIG. 5: *Carrier heating efficiency – dependence on Fermi energy.* **a)** The peak photoconductivity of the sample with controllable Fermi energy as a function of gate voltage for five different excitation powers at excitation wavelength 1500 nm. The corresponding excitation density N_{exc} is given in units of 10^{12} absorbed photons/cm². At gate voltages away from the Dirac point the photoconductivity is negative, while it changes sign upon approaching the Dirac point, in agreement with very recent observations [16, 17]. **b)** The peak photoconductivity as a function of excitation power (N_{exc}) for three gate voltages, corresponding to $N_{int} = 1, 2$ and $3 \cdot 10^{12}$ carriers/cm² (light to dark blue). The solid lines show the results of the model described in the text and the Methods section with a fixed heating efficiency. For a decreasing number of intrinsic carriers (lower Fermi energy) the carrier heating efficiency decreases, in agreement with the slowing down of the rise with decreasing Fermi energy. The symbol size of the data in panels **a** and **b** represents the error.

SUPPLEMENTARY MATERIAL

A. Characterization of the sample with controllable Fermi energy

In order to translate the applied gate voltage V_g into the Fermi energy of the graphene sheet, we determine the capacitive coupling of the weakly doped silicon backgate to the graphene sheet. For this, we use a sample with the same substrate as the sample used for the E_F -dependent measurements, however with graphene shaped as a Hall bar (see bottom right inset of Fig. S2a). We apply a current of $I = 1\mu\text{A}$ in the x -direction and measure the Hall voltage V_H between two contacts in the y -direction. We measure the Hall voltage as a function of backgate voltage for a z -directed magnetic field of both $+0.6\text{ T}$ and -0.6 T , and use the difference between these two scans to account for offsets (from device asymmetry, for example). From the Hall voltage we extract the carrier density *vs.* backgate voltage (see Fig. S1a) using

$$N_{\text{int}} = \frac{I \cdot B}{e \cdot V_H}, \quad (\text{S1})$$

with e the elementary charge. This allows us to extract the capacitance of the backgate, where we find $C = 6.3 \cdot 10^{-5}\text{ F/m}^2$, which is somewhat smaller than the theoretical value for 300 nm oxide: $C_{\text{th}} = 11.6 \cdot 10^{-5}\text{ F/m}^2$. The reason for this could be the low density of carriers in the silicon or the large size of the graphene flake. We use the obtained capacitive coupling to obtain the Fermi level corresponding to the applied gate voltages of the sample. It also allows us to obtain the device mobility, contact resistance and width of the neutrality point through the device resistance as a function of gate voltage. We find a contact resistance of 3.3 k Ω , a neutrality point width of $\Delta = 58\text{ meV}$, and a (lower bound) of the mobility of $\sim 300\text{ cm}^2/\text{Vs}$ (see Fig. S1b). This is in reasonable agreement with the $\sim 700\text{ cm}^2/\text{Vs}$ found from the photoconductivity fits.

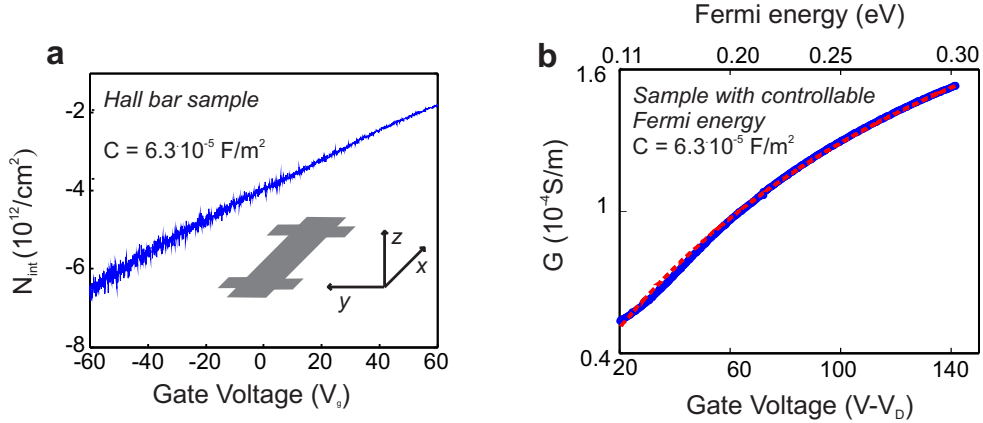


FIG. S1: **a)** The number of intrinsic carriers as a function of gate voltage, extracted from Hall measurements on a similar device as the one used in the Fermi-level dependent measurements, equipped with additional contacts in the Hall geometry. **b)** The device resistance as a function of $(V_g - V_D)$ together with a fit using the determined capacitance, which yields the device mobility, contact resistance and neutrality region width.

B. Characterization of the sample with fixed Fermi energy

We characterize the sample with fixed Fermi energy using Raman spectroscopy with pump wavelength 532 nm (see an exemplary Raman trace in Fig. S2a). The width of the 2D peak of $\sim 33\text{ cm}^{-1}$ shows that the graphene, grown by chemical vapor deposition, is predominantly monolayer. We also extract the Fermi energy, by analyzing the G peak location and the ratio between the 2D and the G peak ($\sim 1585\text{ cm}^{-1}$) and >2 , respectively, for the trace shown in Fig. S2). The Raman spectra of more than 100 traces on different locations on the sample yield an average G peak position of $\sim 1585\text{ cm}^{-1}$, which indicates a Fermi energy of $<0.15\text{ eV}$ [S1, S2]. To get the most realistic estimate for the Fermi energy that corresponds to our optical pump - THz probe experiment, the Raman spectra are taken under

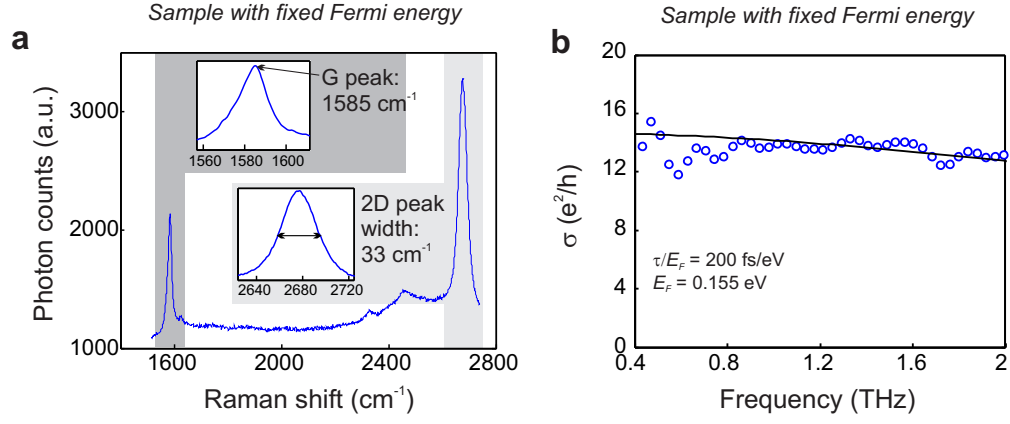


FIG. S2: **a)** Raman spectrum of the sample with fixed Fermi energy. The insets show the G peak and the 2D peak. **b)** The steady state conductivity spectrum of the sample with fixed Fermi energy (without photoexcitation), together with a Drude conductivity fit (black solid line).

very similar environmental conditions (nitrogen flushing).

We further characterize the sample using THz conductivity measurements, where we alternatively measure the substrate with and without graphene in the THz focus. This allows us to obtain the steady state conductivity (without photoexcitation). The results are shown in Fig. S2b together with a conductivity fit as explained in the Methods section. We obtain good agreement between data and model for a Fermi level of $E_F = 0.155$ eV and a scattering time proportionality constant of 200 fs/eV, corresponding to a mobility of ~ 2300 cm²/Vs. We use this scattering time proportionality constant and a slightly lower Fermi energy ($E_F = 0.11$ eV) to compare all optical pump - terahertz probe data measured on this sample to the carrier heating model. The slightly lower Fermi energy follows from the photoconductivity at high fluence in Fig. 4a (given the scattering time proportionality constant of 200 fs/eV), and could be due to spatial variation of the Fermi energy, photo-cleaning during the course of the experiment, or due to a modified humidity during the experiment.

C. Positive photoconductivity at the Dirac point and the Silicon contribution

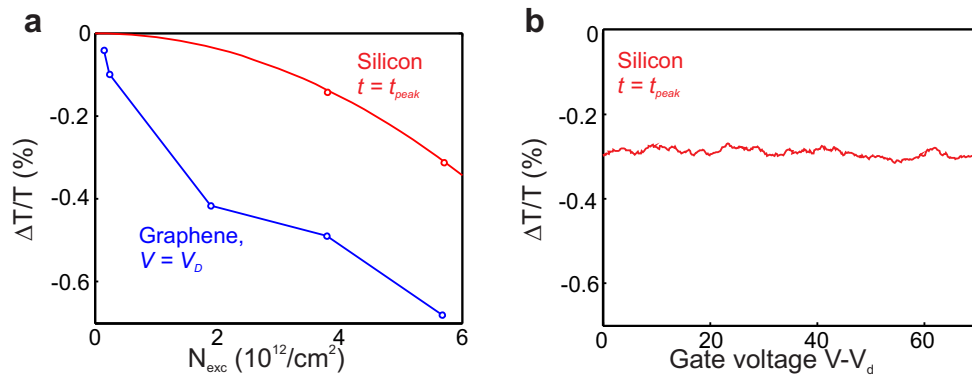


FIG. S3: Pump-probe signal recorded at the pump-probe delay corresponding to the graphene signal peak, measured at the Dirac point (blue) with negative change in transmission (positive conductivity) as a function of absorbed fluence (in the graphene sheet). The same measurement on the substrate without graphene at the same pump-probe delay gives a quadratic signal due to two photon absorption (red).

We use an excitation wavelength of 1500 nm for our pump-probe measurements on the gated graphene sample to avoid exciting electron-hole pairs in the silicon, which would obscure our signal. However, there is a small contribution of two-photon absorption that leads to THz photoconductivity in the silicon, in addition to the photoconductivity of

the graphene sheet. We find that for the lowest fluences the silicon signal is negligible. However due to the quadratic increase with fluence, the silicon signal is not negligible at the highest fluences, in cases where the Fermi energy, and therefore the graphene signal, is very low. In Fig. S3a we show the pump probe signal that originates from the substrate without graphene and the pump probe signal for the substrate with graphene at very low Fermi energy. It is noteworthy to point out that the silicon contribution to the combined graphene-silicon signal is insignificant at gate voltages far away from the Dirac point and that it does not change with gate voltage (see Fig. S3b). Only around the Dirac point, and at the highest fluences, does part of the positive photoconductivity come from the graphene and part from the silicon. Importantly, at low fluence, the positive photoconductivity that we observe stems completely from the graphene, showing the capability of tuning the Fermi energy close enough to the Dirac point to change the sign of the graphene THz photoconductivity. And even at the highest employed fluence, the signal from graphene at the Dirac point is still larger than the signal from the silicon substrate. We corrected the fluence dependent results presented in Fig. 5 of the main paper for this small substrate contribution.

Supplementary References

- [S1] H. Yan et al., Infrared spectroscopy of wafer-scale graphene. *ACS Nano* **5**, 9854–9860 (2011)
- [S2] A. Das et al., Monitoring dopants by Raman scattering in an electrochemically top-gated graphene transistor. *Nature Nanotech.* **3**, 210–215 (2008)